Chinese Chemical Letters 35 (2024) 108331

Contents lists available at ScienceDirect

Chinese Chemical Letters

journal homepage: www.elsevier.com/locate/cclet

Defect reduction to enhance the mechanical strength of nanocellulose carbon aerogel

Haihong Lai[a,1], Zehong Chen[a,1], Hao Zhuo[a], Yijie Hu[a], Xuan Zhao[a], Jiwang Yi[a], Hongzhi Zheng[a], Ge Shi[a], Yifan Tong[a], Ling Meng[b,*], Xinwen Peng[a,*], Linxin Zhong[a,*]

[a] *State Key Laboratory of Pulp and Paper Engineering, South China University of Technology, Guangzhou 510641, China*
[b] *Huangpu Hydrogen Energy Innovation Center/Guangzhou Key Laboratory for Clean Energy and Materials, School of Chemistry and Chemical Engineering, Guangzhou University, Guangzhou 510006, China*

ARTICLE INFO

Article history:
Received 17 November 2022
Revised 27 February 2023
Accepted 9 March 2023
Available online 20 March 2023

Keywords:
Biomass
Cellulose nanofiber
Pyrolysis
Renewable
Carbon aerogel

ABSTRACT

Carbon aerogels prepared from renewable nano building blocks are rising-star materials and hold great promise in many fields. However, various defects formed during carbonization at high temperature disfavor the stress transfer and thus the fabrication of flexible carbon aerogel from renewable nano building blocks. Herein, a structural defect-reducing strategy is proposed by altering the pyrolysis route of cellulose nanofiber. Inorganic salt that inhibits the generation of tar volatilization during pyrolysis can prevent the formation of various structural defects. Microstructure with fewer defects can reduce stress concentration and remarkably enhance the compressibility of carbon aerogel, thus increasing the maximum stress retention of carbon aerogel. The carbon aerogel also has high stress sensor sensitivity and excellent temperature coefficient of resistance. The structural defect-reducing strategy will pave a new way to fabricate high-strength carbon materials for various fields.

Lightweight, compressible and elastic carbon aerogels (CECA) are highly desirable for biological signal monitoring [1,2], flexible electronic skin [3–5], soft robot [6,7], supercapacitor [8–10] and catalyst support [11,12]. CECA fabricated from renewable resource represent a new type of substitution to carbon nanotube (CNT) and graphene aerogels due to the low cost and environmental friendless of raw materials. Cellulose nanofiber (CNF) as a renewable nano building block derived from various plants is abundant, low-cost, and mechanically strong [13–15]. Owing to its high aspect ratio and abundant functional groups, CNF can directly self-assemble as or be used to crosslink other building blocks into lightweight aerogels, which can be further annealed to prepare carbon aerogels. This type of CNF carbon aerogel has been applied in various fields including energy [16,17], catalysis [18], and electromagnetic interference shielding [19]. However, the serious structural shrinkage of CNF aerogel during pyrolysis leads to uncontrollable microarchitecture and low mechanical strength (*e.g.*, poor compressibility and elasticity). Therefore, compressibility and elasticity are the main challenges that CNF carbon aerogel faced.

In order to enhance the mechanical properties of CNF carbon aerogel, additional components with high carbon content such as RGO (reduced graphene oxide), CNT [8] or lignin [20] were employed to reduce the volume shrinkage and thus enhance the structural stability of CNF carbon aerogel. For example, Liu *et al.* [8] prepared an aerogel with honeycomb structure by using CNF, CNT and RGO. Chen *et al.* [20] demonstrated that the lignin could compensate for the carbon loss of CNF during pyrolysis and thus reduce the volume shrinkage of carbon aerogel, resulting in higher mechanical strength. Although additional nano carbons or carbon sources can merely reduce the volume shrinkage of CNF carbon aerogel in macroscopic scale, it cannot solve the inherent serious carbon loss and structural change of individual CNF.

Structural defects will remarkably affect the mechanical strength of materials. It is inevitable for CNF to form various structural defects during pyrolysis because of the serious carbon loss. CNF is unstable during pyrolysis and will decompose violently to release CO_2, CO, alcohols, ketones, and other carbon-containing substances with low molecular weight, resulting in a high element (especially C) loss [21–23]. Usually, CNF will lose up to 80%–90% of its mass during pyrolysis, depending on the temperature [21,23]. The mass loss inevitably leads to various structural defects such as nanopores, cracks and sp^3 hybrid carbon for CNF-derived carbon aerogel [24,25]. These defects in CNF carbon aerogel will cause

---

[*] Corresponding authors.

E-mail addresses: mengling@gzhu.edu.cn (L. Meng), fexwpeng@scut.edu.cn (X. Peng), lxzhong0611@scut.edu.cn (L. Zhong).

[1] These authors contributed equally to this work.

https://doi.org/10.1016/j.cclet.2023.108331
1001-8417/

Table 1
The element analysis results of CNF aerogels and CNF carbon aerogels.

Samples	Element analysis (wt%)				C/H ratio
	C	H	N	S	
CNF-A	34.43	5.624	0.00	0.055	6.1210
P-CNF-A	31.06	5.582	0.84	0.023	5.5645
CNF-CA	40.60	1.806	0.15	0.232	22.4752
P-CNF-CA	50.62	0.575	0.70	0.154	88.0678

poor stress transfer or stress concentration in the internal structure, thus giving up to poor mechanical performances of the carbon aerogel. It is also reported that sp^2 hybrid carbon is flexible due to its sliding ability, while the sp^3 hybrid carbon connected by covalent bonds may cause severe brittleness and poor flexibility because of its limited slip ability [26]. Thus, it is expected that the reduction of sp^2 hybrid carbon content will also lead to brittle carbon aerogel. The mechanical properties of CNF carbon aerogel will be intrinsically improved if the defects could be reduced. However, to the best of our knowledge, the effective method to address this issue has not been reported.

Herein, we propose an effective strategy to reduce the mass loss of CNF during pyrolysis, and thus significantly decrease defects in the carbon aerogel without supplementing additional carbon source or nano carbon. It is found that the addition of inorganic salts such as $NH_4H_2PO_4$ can increase the char yield by reducing the volatilization of tar products, thereby decreasing the structural defects (*i.e.*, pores, cracks, sp^3 hybrid carbon) and finally improving the mechanical property of CNF carbon aerogel. The modified CNF carbon aerogel can maintain 86.9% stress retention and show low plastic deformation (10.8%) during 10000 cycles compression at 50% strain, which enables the carbon aerogel to possess promising stress sensing performances with a high sensitivity. This work provides a unique strategy to regulate various micro defects in carbon materials from abundant biomass to form advanced flexible carbon aerogel.

As shown in Fig. S1 (Supporting information), CNF carbon aerogel was fabricated by directional freezing, freeze-drying, and carbonization. CNFs obtained by TEMPO-mediated oxidation and high-pressure homogenization possess high aspect ratio (Fig. S2a in Supporting information), and the carboxyl content is detected to be 0.948 mmol/g *via* conductometric titration (Fig. S2b in Supporting information). CNFs were firstly dispersed in various inorganic salt ($NH_4H_2PO_4$, $(NH_4)_2SO_4$, NH_4Cl, NaH_2PO_4, $FeCl_3$ and H_3BO_3) solutions. Then, during the directional freezing process, CNFs were expelled by the directionally growing ice to form aligned and continuous lamellar structure (Fig. S1). The formation of such lamellar structure can be ascribed to the large aspect ratio of CNFs and abundant hydrogen bonding among CNFs [27].

Char yield, volume retention, and apparent density can directly indicate the mass loss and structure shrinkage of CNF aerogels after carbonization. As shown by the thermogravimetric (TG) analysis in Figs. 1a–c and Fig. S3 (Supporting information), the char yields of aerogels with $NH_4H_2PO_4$ (P-CNF-A, 38.0%), $(NH_4)_2SO_4$ (S-CNF-A, 18.8%), NH_4Cl (Cl-CNF-A, 20.8%), NaH_2PO_4 (Na-CNF-A, 33.1%), $FeCl_3$ (Fe-CNF-A, 21.8%), and H_3BO_3 (B-CNF-A, 29.7%) are higher than that of pure CNF aerogel (CNF-A, 16.5%). Particularly, P-CNF-A has the highest char yield among the selected inorganic salts. Therefore, $NH_4H_2PO_4$ is selected as a high-efficiency inorganic salt to fabricate CNF carbon aerogel. The carbon content (50.62 wt%) of P-CNF-CA is also higher than that of CNF-CA (40.60 wt%) based on element analysis (Table 1). The results confirm that $NH_4H_2PO_4$ reduces the loss of element carbon. The macroscopic and microscopic structure of P-CNF-CA (carbon aerogel with $NH_4H_2PO_4$) is also significantly different from that of CNF-CA. CNF-CA maintains only 8.48% volume after annealing (Fig. S4 in Supporting information). However, the volume retention of P-CNF-CA is as high as 23.9%. The apparent density of P-CNF-CA is 11.9 mg/cm^3, only slightly higher than that of P-CNF-A (9.48 mg/cm^3). CNF-CA, however, has a high density of 18.3 mg/cm^3, which is much higher than that of CNF-A (7.04 mg/cm^3). Meanwhile, the macroscopic structure of P-CNF-CA at high temperature (being grilled in flame for 10 s) is more intact than that of CNF-CA (structure is destroyed after 7 s) (Fig. S5 in Supporting information). These results indicate that the CNF aerogel with $NH_4H_2PO_4$ and its carbon aerogel have enhanced thermal stability.

The microstructures of CNF aerogels and carbon aerogels are shown in Figs. 1d–g, Figs. S6 and S7 (Supporting information). The lamella of CNF-CA undergoes severe shrinkage and crimp after annealing (Fig. S6c). However, P-CNF-CA remains the same lamellar structure as that of aerogel before annealing (Fig. S6d), indicating that the high char yield ensures the intact lamellar structure. Many holes and cracks appear on the surface of CNF-CA lamellas (Fig. 1d and Fig. S7a), while almost no hole or crack can be observed on the surface of P-CNF-CA lamellas (Fig. 1e and Fig. S7b). Furthermore, CNF-CA lamella shows many bright spots with a diameter of less than 10 nm, indicating the existence of micropores and mesopores on the lamellar surface (Fig. 1f), which is contrary to the less nanopores on P-CNF-CA lamella (Fig. 1g).

To further give an insight into the structural defects of the two carbon aerogels, more information about mesopore and micropore is revealed by nitrogen adsorption-desorption analysis. The specific surface area of CNF-CA is 215.0 m^2/g, much higher than that of P-CNF-CA (88.7 m^2/g, Fig. S8 in Supporting information). Although the pore sizes of CNF-CA and P-CNF-CA mainly concentrate at around 1.27 nm (Fig. 1h), the microporous volume of CNF-CA (0.0705 cm^3/g) is much higher than that of P-CNF-CA (0.0258 cm^3/g). These results demonstrate that directly annealing CNF aerogel causes not only a large number of holes and cracks, but also abundant mesopores and micropores. By adding $NH_4H_2PO_4$, these structural defects are significantly reduced.

More information on the chemical structure and graphitized structure is revealed by Raman, FTIR, and XPS. In the FTIR spectra of CNF aerogels, a wide and broad peak at 3460 cm^{-1} is attributed to the stretching vibrations of hydroxyl groups, while the peak at 1629-1614 cm^{-1} corresponds to the sodium carbonyl groups (Fig. S9a in Supporting information) [28–30]. As compared with CNF-A, the peak of hydroxyl groups in P-CNF-A shifts to a higher wavenumber (from 3405 cm^{-1} to 3420 cm^{-1}), indicating the formation of hydrogen bonds between phosphate groups and hydroxyl groups. After carbonization, P-CNF-CA shows an additional peak at 908 cm^{-1} corresponding to P-O-H [31], demonstrating the successful phosphorylation modification of P-CNF-CA (Fig. S9b in Supporting information). As shown in P 2p spectrum in XPS (Fig. S10 in Supporting information), the fitting peaks at 132.8 eV and 133.6 eV can be assigned to P-C bonding and pyrophosphate, respectively [32]. The introduction of thermo-oxidative stable P=O/P-O bonds can reduce the carbon active sites and structure destroy of CNF carbon aerogel at high temperature [32].

In theory, sp^2 C constructs the turbostratic graphene sheets, while sp^3 C indicates the cross-bridge among the graphene sheets [33,34]. P-CNF-CA (Fig. 1j) has a higher sp^2 C content (71.0 at%) than CNF-CA (45.1 at%, Fig. 1i), while the sp^3 C content of P-CNF-CA (14.7 at%) is lower than that of CNF-CA (36.8 at%). These results indicate that $NH_4H_2PO_4$ can increase the concentration of sp^2 C during pyrolysis. The graphitization degrees of CNF-CA and P-CNF-CA were further characterized by X-ray diffraction (XRD) patterns (Fig. S11 in Supporting information) and Raman spectroscopy (Fig. 1k). The XRD pattern of CNF-CA reveals a broad diffraction peak centered at $2\theta = 23.3°$, representing the (002) peak of the ordered graphitelike structure (Fig. S11). The (002) peak position of

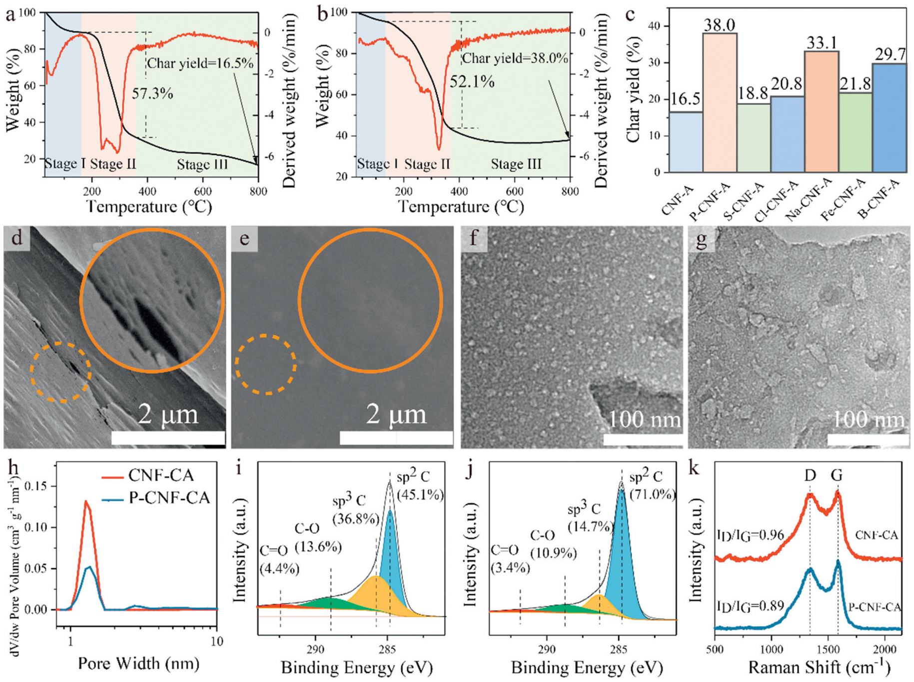

Fig. 1. TG and DTG curves of (a) CNF-A and (b) P-CNF-A. (c) Char yield of CNF-A, P-CNF-A, S-CNF-A, Cl-CNF-A, Na-CNF-A, Fe-CNF-A and B-CNF-A in thermogravimetric analysis. SEM images of the lamellas from (d) CNF-CA and (e) P-CNF-CA. TEM images of the lamellas from (f) CNF-CA and (g) P-CNF-CA. (h) Pore size distributions of CNF-CA and P-CNF-CA based on original density functional theory. C 1s spectra of (i) CNF-CA and (j) P-CNF-CA. (k) The Raman spectra of CNF-CA and P-CNF-CA.

P-CNF-CA slightly shifts to a larger angle ($2\theta = 25.2°$), indicating a decreasing interlayer space (d_{002}) of the graphite microcrystal. The Raman spectra of carbon aerogels reveal two prominent peaks at 1343.1 and 1586.9 cm^{-1}, corresponding to the disordered (D) and graphitic (G) bands, respectively [35,36]. I_D/I_G is inversely proportional to the in-plane size of the sp^2 C building blocks (La) [37]. The I_D/I_G of P-CNF-CA is 0.89, which is lower than that of CNF-CA ($I_D/I_G = 0.96$), indicating a higher graphitization degree and sp^2 C content of P-CNF-CA.

Above results clearly demonstrate that various defects, including holes, cracks, mesopores, micropores, and sp^3 hybrid carbon, will be produced during CNF annealing due to the significant mass loss. $NH_4H_2PO_4$ can significantly reduce carbon loss and defects, but the change in pyrolysis route needs to be further clarified to understand the defect-forming and defect-reducing mechanisms.

Generally, cellulose is carbonized to form char through dehydration, thermal scission, and aromatization of carbon residue [21,38]. The incorporation of phosphoric acid, carboxyl or metal ions catalyzes the decomposition of cellulose and promotes the formation of carbon [21,29,30]. At the same time, volatiles (containing gas and tar) appear via other main pyrolysis route, resulting in the decrease of char yield. The addition of $NH_4H_2PO_4$ results in high char yield and different structures, indicating that the pyrolysis route of CNF is changed, and accordingly the products (*i.e.*, char, tar and volatiles) are altered. Therefore, the pyrolysis products of CNF-CA and P-CNF-CA were analyzed to figure out the reasons behind the increase of char yield and reduce of structural defects. The pyrolysis products were characterized by TG-FTIR and TG-gas chromatography-mass spectrometry (TG-GC-MS) from volatiles. The pyrolysis process of P-CNF-A can be divided into three stages: the evaporation of physically adsorbed water (stage I, <134 °C), devolatilization (stage II, 134–368 °C), and the char residues formation (stage III, >368 °C) (Fig. 1b). CNF-A also undergoes similar pyrolysis stages as shown in Fig. 1a. In stage II, P-CNF-A loses 52.1% mass, which is less than that of CNF-A (57.3%), demonstrating that $NH_4H_2PO_4$ can reduce the formation of volatiles. It can be attributed to the phosphorylation at C-6 hydroxyl groups, dehydration and condensation of cellulose caused by the $NH_4H_2PO_4$ during pyrolysis [39]. The maximum rate of mass loss indicates the maximum decomposition rate and volatile formation rate at a certain temperature. The maximum rate of mass loss occurs at around 327 °C for P-CNF-A and is higher than that of CNF-A (290 °C) at stage II, confirming that $NH_4H_2PO_4$ can delay the formation of volatiles and change the pyrolytic route.

The TG-FTIR indicates the changes in volatiles of CNF-A and P-CNF-A during pyrolysis (Figs. 2a and b). The absorbance intensity at a specific wavenumber is linearly dependent on the relative concentration of the volatiles. CO_2 is the major gaseous product of cellulose pyrolysis and is primarily generated via the decarboxylation reaction and the release of carboxyl groups [22]. The bands at 2360 cm^{-1} (corresponding to O=C=O) in the spectrum of CNF-A is prominent at 309 °C (Fig. 2a), exhibiting that CNF-A decomposes violently into CO_2 at this temperature. In contrast, the peak for O=C=O band in the spectrum of P-CNF-A is at 383 °C (Fig. 2b), which is remarkably higher than that of CNF-A (309 °C). These results again demonstrate that $NH_4H_2PO_4$ can delay the formation of volatiles and thus increase char yield. According to TG-FTIR, $NH_4H_2PO_4$ not only can delay the formation of CO_2, but also change the components of volatiles. In order to investigate the effect of $NH_4H_2PO_4$ on CNF volatile components, the pyrolytic products of CNF-A and P-CNF-A at DTG peak temperature were further studied by TG-GC-MS. As shown in Fig. 2c, various organic compounds such as levoglucosan (LG, the main monosaccharide derivatives), levoglucosenone (LGO) and furan compounds are formed during pyrolysis of CNF-A. However, almost no characteristic peak of LG can be detected in P-CNF-A, indicating that $NH_4H_2PO_4$ can inhibit the formation of LG.

To the best of our knowledge, the anhydroglucose unit in cellulose has two main competing dehydration routes (Fig. S12 in Supporting information) [40,41]. In path 1, thermal scission happens without the dehydration of anhydroglucose unit, leading to the formation of tar volatilization. In path 2, the anhydroglucose units

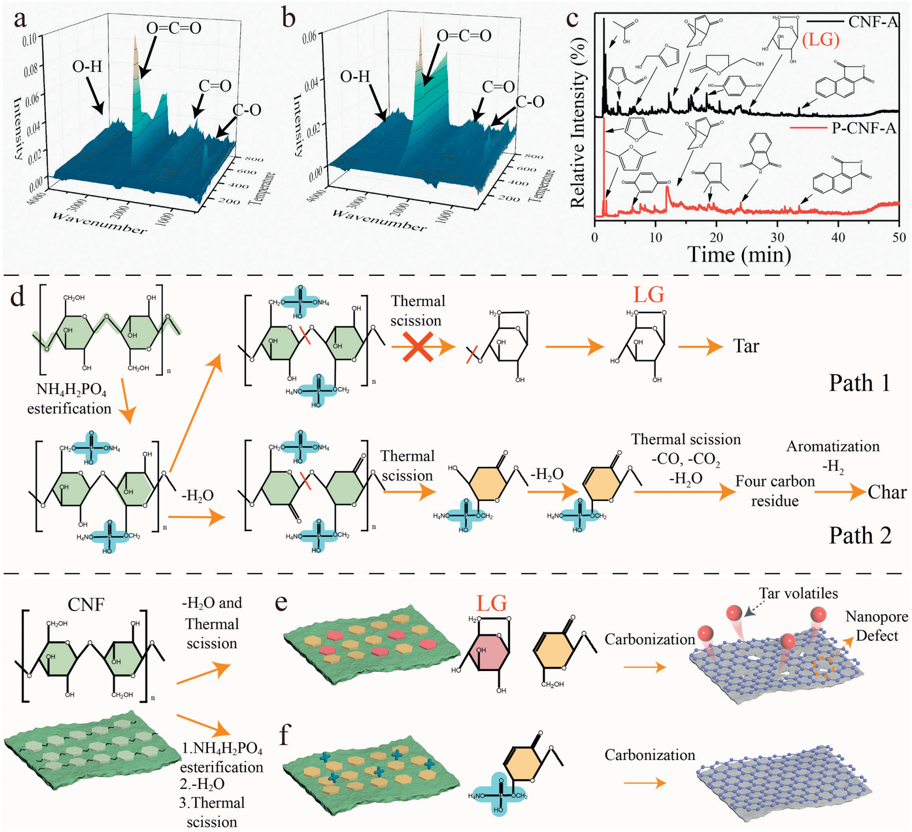

Fig. 2. The pyrolysis route of CNF aerogels during annealing. The TG-FTIR of the pyrolytic gas products for (a) CNF-CA and (b) P-CNF-CA. (c) Gas chromatograms of the pyrolytic products for CNF-A and P-CNF-A at DTG peak temperature. (d) Pyrolysis route of P-CNF-A in the carbonization process. Schematic illustration of defect formation and suppression during pyrolysis of (e) CNF-A and (f) P-CNF-A.

dehydrate before thermal scission, which facilitates the generation of char. According to the above analysis, it is speculated that the path 1 in P-CNF-A is suppressed during pyrolysis. Specifically, in the path 1, the thermal scission between two anhydroglucose units needs the participation of hydroxyl in -CH_2OH. $NH_4H_2PO_4$ reacts with -CH_2OH in the anhydroglucose unit to suppress the thermal scission in path 1, thus inhibiting the formation of intermediate products (such as LG, as confirmed by TG-GC-MS) and the final tar. As a result, more anhydroglucose units are pyrolyzed through the path 2, in which the intermediate products mainly form the four carbon residues through removing CO, CO_2 and H_2O. The four-carbon residues further form char through removing H_2 and aromatization (path 2 in Fig. 2d).

Based on the above results, we put forward the mechanism of structural defect reduce by adding $NH_4H_2PO_4$ during pyrolysis. As shown in Fig. 2e, severe thermal scission occurs to CNF without $NH_4H_2PO_4$. The intermediate products (such as LG) in path 1 mainly produce tar volatilization, which results in many defects such as micropores and mesopores, and thus giving rise to char with low graphitization degree. However, with $NH_4H_2PO_4$, the thermal scission molecules are converted into char during pyrolysis (Fig. 2f). The esterification of $NH_4H_2PO_4$ with C6 in anhydroglucose inhibits the cyclization reaction to generate LG in path 1, thus restraining the formation of tar (Fig. 2f). Therefore, $NH_4H_2PO_4$ can improve char yield and reduce tar volatilization by changing the pyrolysis routes, which finally inhibit the formation of defects such as holes, cracks, pores, and sp^3 hybrid carbon.

To figure out the influence of defect on the mechanical performances of carbon aerogel, compressing tests were carried out. Irreversible deformation occurs to CNF-CA after 100 compression cycles at 90% strain (the inset of Fig. 3a), and the maximum stress retention is 52.3% (Fig. 3a). By contrast, P-CNF-CA can almost retain its original shape (the inset of Fig. 3b) and has a higher stress retention of 65.7% after 100 cycles at 90% strain (Fig. 3b). The lamellas of CNF-CA and P-CNF-CA after compressing for 100 cycles at 90% strain are shown in Figs. 3e and f. Fracture happens to the lamella of CNF-CA, caused by stress concentration around holes and cracks (Fig. 3e). In contrast, P-CNF-CA remains the intact lamella after 100 cycles at 90% strain (Fig. 3f). To investigate the influencing mechanism of the structural defects on the compressibility, finite element simulation was carried out. As shown in structural model of CNF-CA, the holes on the surface of lamella will cause the stress concentration and result in fragile structure during compression (Fig. 3i). However, the stress on the model of P-CNF-CA can effectively transfer (Fig. 3j), demonstrating that intact lamellar structure with fewer holes, cracks, micropores, and mesopores can reduce stress concentration during compression and thus give rise to higher mechanical strength. Moreover, the higher sp^2 hybrid carbon content and lower sp^3 hybrid carbon content can improve the inherent flexibility and reduce brittleness of carbon lamellas. Meanwhile, P-CNF-CA can be cyclically compressed and rebound at low (liquid nitrogen, Fig. S13a in Supporting information) or high temperature (alcohol lamp flame, Fig. S13b in Supporting information), indicating its high mechanical performances in extreme environment.

The fatigue resistance of P-CNF-CA was further tested at 50% strain for 10000 cycles (Fig. 3c). The stress-strain curve at 10000th cycle is similar to that of the first cycle. P-CNF-CA can maintain high stress retention (86.9%) and show only 10.8% plastic deformation (Fig. 3d), indicating excellent fatigue resistance. After being compressed at 50% for 10000 cycles, the lamellas of P-CNF-CA can be well maintained, without apparent cracks on the lamellar

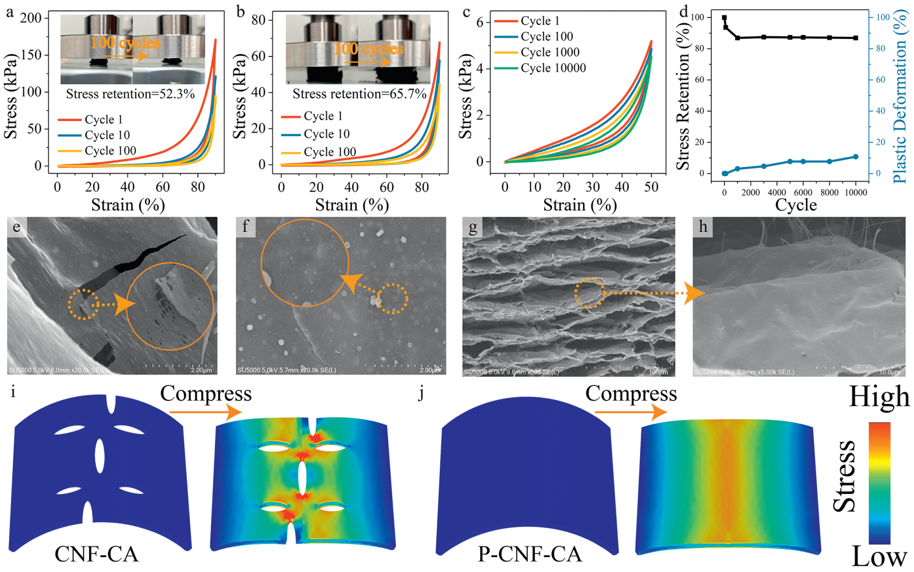

Fig. 3. Stress-strain curves and digital photographs of (a) CNF-CA and (b) P-CNF-CA at 90% strain for 100 cycles. (c) Stress-strain curves of P-CNF-CA at 50% strain for 10000 cycles. (d) Compression stress retention and plastic deformation of P-CNF-CA during 10000 cycles at 50% strain. The SEM images of (e) CNF-CA and (f) P-CNF-CA after being compressed for 100 cycles at 90% strain. SEM images of mesoscopic (g) lamellar structure and (h) lamellar surface from P-CNF-CA after 10000 compression cycles at 50% strain. Finite element models of (i) CNF-CA (a lamella with holes) and (j) P-CNF-CA (a lamella without hole) upon compression.

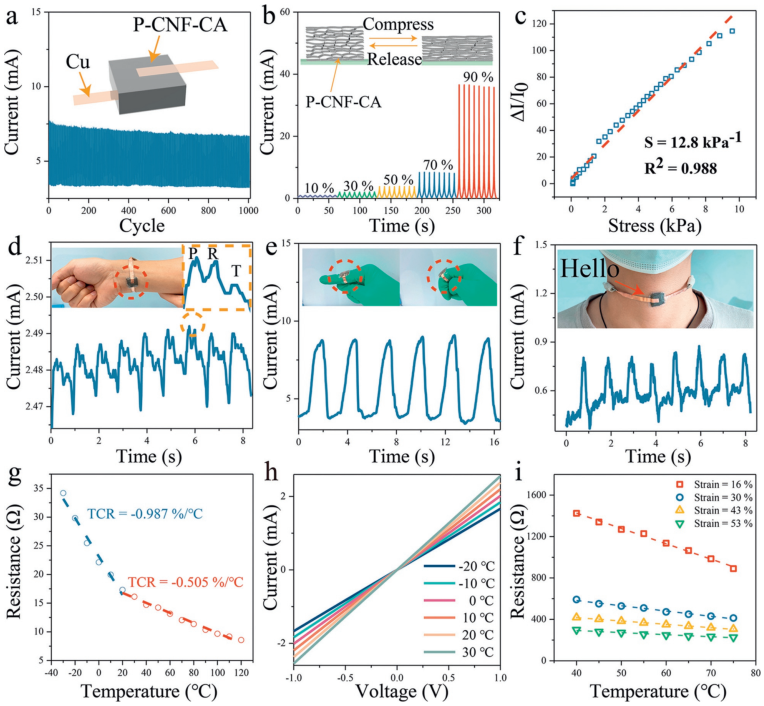

Fig. 4. (a) Current stability at 10% strain for 1000 cycles. Inset: a schematic of sensor assembled from P-CNF-CA. (b) Real-time currents at different compressive strains. Inset: schematic of lamellar structure change from P-CNF-CA during compression. (c) Linear sensitivity in a wide pressure range of 0.1–9.6 kPa. Current signals from (d) human arm pulse, (e) bending finger, and (f) speaking "Hello". (g) The temperature coefficient of resistance (TCR) for P-CNF-CA. (h) Current varies with the voltage from -2 V to 2 V at different temperatures. (i) Thermal sensitivity curves of encapsulated P-CNF-CA at different strains.

surface (Figs. 3g and h), suggesting the high structural stability of P-CNF-CA.

Encouraged by its aligned lamellar structure and mechanical robustness, P-CNF-CA can be considered as a promising candidate for piezoresistive sensor. P-CNF-CA was encapsulated between two PE films with copper electrodes to act as a sensor (the inset of Fig. 4a). The fatigue-resistant structure of P-CNF-CA ensures the stable and regular output-current signals at 10% strain for 1000 cycles (Fig. 4a) and at 70% strain for 850 cycles (Fig. S14a in Supporting information). P-CNF-CA also shows regular output of current at various strains (Fig. 4b). The current rises continuously with increasing pressure or strain (Figs. S14b and c in Supporting information). When being compressed, the conductivity of the carbon aerogel is improved since adjacent lamellas contact to form more conductive paths along the compression direction (the inset of Fig. 4b). To evaluate and quantify the sensing properties of P-CNF-CA, sensitivity (S, the linear relationship between applied pressure and current change) and gauge factor (GF, the linear relationship between applied strain and resistance change) were calculated. As shown in Fig. 4c, the sensor shows a high sensitivity of 12.8 kPa^{-1} with good linear relationship ($R^2 = 0.988$) in a wide pressure (0.1–9.6 kPa, equates to 2.5%–68% strain), which is superior to those of many other pressure sensors, such as GO-based carbon sponge [42,43], CNT-based elastomer [44], and MXene-based textile or aerogel (Table S1 in Supporting information) [45–47]. Meanwhile, the detection limit of the sensor is low to 29 Pa (Fig. S14d in Supporting information) and the sensitivity is 1.88 kPa^{-1} at a tiny stress of 0-290 Pa (Fig. S14e in Supporting information), which ensures the signal capture of small pressure. Within 10.9% strain, resistance response ($\Delta R/R_0$) increases rapidly and linearly with a GF high up to 13.5 (Fig. S14f in Supporting information). The current response of P-CNF-CA at extremely low and high temperatures was further analyzed. It shows stable current response when the carbon aerogel is compressed on a liquid nitrogen refrigeration platform and heating stage in air at 50% strain for 100 cycles (Figs. S15a and b in Supporting information).

Due to the stable and highly sensitive stress-current response performances, P-CNF-CA was assembled into a wearable sensor to detect stress variations caused by slight movements of human body. When the sensor is worn on the human wrist, it can detect slight and regular signals from fluctuant pulse with an interval pulse of about 0.93 s including three characteristic peaks from different intensities of pulses (Fig. 4d). As the finger bends and straightens, the current signal fluctuates up and down repeatedly (Fig. 4e). The sensor can also detect the slight motion of skin by speaking the word “Hello” with two characteristic peaks, when the sensor is attached to the human throat (Fig. 4f).

Furthermore, it is found that the resistance decreases with increasing temperature (Fig. 4g), indicating that P-CNF-CA is a negative temperature coefficient (NTC) thermistor. As the dynamic resistance response shown in Fig. 4g, P-CNF-CA displays a good sensitivity in a wide temperatures range (-30–20 °C, TCR = -0.987%/°C, 20-120 °C, TCR = -0.505%/°C). The charge transport in P-CNF-CA mainly occurs through the carbon structure transport (such as carrier hopping). The rising of ambient temperature will increase the carrier density, leading to higher conductivity [48]. The current and voltage change linearly when the temperature is constant (Fig. 4h), which reveals the thermal sensor has a stable output at a constant temperature. To explore the influence of compression degree on the temperature sensitivity, the temperature-induced resistance changes of P-CNF-CA at different compressive strains were further tested. As shown in Fig. 4i, the resistance at the initial temperature and the sensitivity at different strains decrease with increasing strain. The sensitivities of the thermal sensor at 16%, 30%, 43% and 53% compressive strain is -1.07, -0.864, -0.759, -0.629%/°C, respectively, indicating the sensitivity of P-CNF-CA can be easily adjusted by changing the strain of P-CNF-CA. Considering its thermal sensitivity, the sensor also can be explored in detecting the change of temperature. As shown in Fig. S16 (Supporting information), the resistance of the thermal sensor decreases from 430 Ω to 288 Ω as the thermal sensor is placed from room temperature (30 °C) to the hot water (90 °C). Then the resistance rises steadily with the dropping temperature of hot water.

In summary, CNF is thermal instability during pyrolysis because the directly thermal scission produces large amounts of intermediates and thus tar volatilization, leading to many defects of carbon aerogels. To this end, a structural defect-reducing approach is proposed by altering the pyrolysis route of CNF. The esterification of $NH_4H_2PO_4$ with C6 in anhydroglucose inhibits the formation of intermediates and the volatilization of resultant tar, thus restraining the formation of various defects including holes, cracks, micropores, mesopores, and sp^3 hybrid carbon. The mechanical stability and fatigue resistance of the CNF carbon aerogel with $NH_4H_2PO_4$ has been significantly enhanced, since the decreasing structural defects can effectively reduce stress concentration. These advantages endow the carbon aerogel with highly sensitive piezoresistive response (sensitivity = 12.8 kPa^{-1}) and excellent temperature coefficient of resistance (TCR= -0.987%/°C), ensuring the stable use in flexible sensor, especially pressure sensor, temperature sensor, and aerospace sensor.

Declaration of competing interest

The authors declare that they have no known competing financial interests or personal relationships that could have appeared to influence the work reported in this paper.

Acknowledgments

The authors acknowledge the National Natural Science Foundation of China (Nos. 32201499, 22208069 and 32071714), Guangdong Basic and Applied Basic Research Foundation (No. 2021A1515110205), Fundamental Research Funds for the Central Universities (No. 2022ZYGXZR019), and the State Key Laboratory of Pulp & Paper Engineering (No. 2022C01).

Supplementary materials

Supplementary material associated with this article can be found, in the online version, at doi:10.1016/j.cclet.2023.108331.

References

[1] X. Wang, Z. Liu, T. Zhang, Small 13 (2017) 1602790.
[2] Y. Feng, H. Liu, W. Zhu, et al., Adv. Funct. Mater. 31 (2021) 2105264.
[3] W.D. Li, K. Ke, J. Jia, et al., Small 18 (2022) 2103734.
[4] Y. Guo, X. Wei, S. Gao, et al., Adv. Funct. Mater. 31 (2021) 2104288.
[5] L. Lu, B. Yang, J. Liu, Chem. Eng. J. 400 (2020) 125928.
[6] M. Xie, M. Zhu, Z. Yang, S. Okada, S. Kawamura, Nano Energy 79 (2021) 105438.
[7] S. Chen, A. Surendran, X. Wu, W.L. Leong, Adv. Funct. Mater. 30 (2020) 2006186.
[8] H. Liu, T. Xu, C. Cai, et al., Adv. Funct. Mater. 32 (2022) 2113082.
[9] S. Long, Y. Feng, F. He, et al., Nano Energy 85 (2021) 105973.
[10] S. Sun, F. Han, X. Wu, Z. Fan, Chin. Chem. Lett. 31 (2020) 2235–2238.
[11] H. Zhao, Y. Wang, Y. Wang, T. Cao, G. Zhao, Appl. Catal. B: Environ. 125 (2012) 120–127.
[12] H. Li, X. Shu, P. Tong, et al., Small 17 (2021) 2102002.
[13] Z. Zeng, E. Mavrona, D. Sacré, et al., ACS Nano 15 (2021) 7451–7462.
[14] X. Han, Z. Wang, L. Ding, et al., Chin. Chem. Lett. 32 (2021) 3105–3108.
[15] Z. Zhang, Z. Yao, Z. Jiang, Chin. Chem. Lett. 32 (2021) 3575–3578.
[16] Q. Zhang, C. Chen, W. Chen, et al., ACS Appl. Mater. Inter. 11 (2019) 5919–5927.
[17] Y. Chen, Y. Hu, J. Chen, et al., Colloids Surfaces A: Physicochem. Eng. Asp. 626 (2021) 127003.
[18] R. Cao, L. Li, P. Zhang, J. Hazard. Mater. 407 (2021) 124793.
[19] Y. Fei, M. Liang, L. Yan, Y. Chen, H. Zou, Chem. Eng. J. 392 (2020) 124815.
[20] Z. Chen, H. Zhuo, Y. Hu, et al., Adv. Funct. Mater. 30 (2020) 1910292.
[21] E. Frank, L.M. Steudle, D. Ingildeev, J.M. Spörl, M.R. Buchmeiser, Angew. Chem. Int. Ed. 53 (2014) 5262–5298.
[22] F. Liang, R. Wang, X. Hongzhong, et al., Bioresour. Technol. 256 (2018) 53–60.
[23] Y. Eom, S.M. Son, Y.E. Kim, et al., Carbon 150 (2019) 142–152.
[24] A. Tomczyk, Z. Sokołowska, P. Boguta, Rev. Environ. Sci. Biotechnol. 19 (2020) 191–215.
[25] L. Zhao, W. Zheng, X. Cao, Chem. Eng. J. 250 (2014) 240–247.
[26] C. Ding, L. Huang, X. Yan, et al., Adv. Funct. Mater. 30 (2020) 1907486.
[27] W. Chen, H. Yu, S.Y. Lee, et al., Chem. Soc. Rev. 47 (2018) 2837–2872.
[28] N. Lin, C. Bruzzese, A. Dufresne, ACS Appl, Mater. Interface 4 (2012) 4948–4959.
[29] B. Gao, J. Yang, Y. Chen, S. Zhang, Compos. Part B: Eng. 225 (2021) 109253.
[30] B. Gao, J. Yang, S. Zhang, X. Li, Cellulose 28 (2021) 8405.
[31] M. Ghanadpour, F. Carosio, P.T. Larsson, L. Wågberg, Biomacromolecules 16 (2015) 3399–3410.
[32] Y. Feng, B. Wang, X. Li, et al., Carbon 146 (2019) 650–659.
[33] Z.L. Yu, B. Qin, Z.Y. Ma, et al., Adv. Mater. 31 (2019) 1900651.
[34] Z.L. Yu, S. Xin, Y. You, et al., J. Am. Chem. Soc. 138 (2016) 14915–14922.
[35] Y.C. Lee, Y.F. Li, S.L. Lo, et al., Chem. Eng. J. 430 (2022) 132900.
[36] Y. Tao, M. Endo, K. Kaneko, J. Am. Chem. Soc. 131 (2009) 904–905.
[37] C. Hu, S. Sedghi, A. Silvestre-Albero, et al., Carbon 85 (2015) 147–158.
[38] H. Zhuo, Y. Hu, Z. Chen, et al., ACS Sustain. Chem. Eng. 8 (2020) 11921–11929.
[39] G. Dobele, D. Meier, O. Faix, et al., J. Anal. Appl. Pyrol. 58-59 (2001) 453–463.
[40] M.M. Tang, R. Bacon, Carbon 2 (1964) 211–220.
[41] A.G. Dumanlı, A.H. Windle, J. Mater. Sci. 47 (2012) 4236–4250.

[42] F.A. Khan, C.M. Ajmal, S. Bae, et al., Small 14 (2018) 1800549.
[43] H. Chen, G. Sun, Z. Yang, et al., Compos. Sci. Technol. 218 (2022) 109179.
[44] Y. Song, H. Chen, X. Chen, et al., Nano Energy 53 (2018) 189–197.
[45] T. Li, L. Chen, X. Yang, et al., J. Mater. Chem. C 7 (2019) 1022–1027.
[46] Z. Chen, Y. Hu, H. Zhuo, et al., Chem. Mater. 31 (2019) 3301–3312.
[47] R. Liu, J. Li, M. Li, et al., ACS Appl. Mater. Interface 12 (2020) 46446–46454.
[48] Z. Chen, D. Zhao, R. Ma, et al., J. Mater. Chem. B 9 (2021) 1941–1964.